



Next-generation Surgical Navigation: Marker-less Multi-view 6DoF Pose Estimation of Surgical Instruments

Jonas Hein^{a,b}, Nicola Cavalcanti^a, Daniel Suter^c, Lukas Zingg^c, Fabio Carrillo^{a,d}, Lilian Calvet^d, Mazda Farshad^c, Nassir Navab^c, Marc Pollefeys^b, Philipp Fürnstahl^{a,d}

^aResearch in Orthopedic Computer Science, Balgrist University Hospital, University of Zurich, Zurich, Switzerland

^bComputer Vision and Geometry Group, ETH Zurich, Switzerland

^cBalgrist University Hospital, University of Zurich, Switzerland

^dOR-X Translational Center for Surgery, Balgrist University Hospital, University of Zurich, Zurich, Switzerland

^eComputer Aided Medical Procedures, Technical University Munich, Germany

ARTICLE INFO

Article history:

2000 MSC: 41A05, 41A10, 65D05, 65D17

Keywords: Multi-view RGB-D Video Dataset, Marker-less Tracking, Surgical Instruments, Object Pose Estimation, Surgical Navigation, Deep Learning

ABSTRACT

State-of-the-art research of traditional computer vision is increasingly leveraged in the surgical domain. A particular focus in computer-assisted surgery is to replace marker-based tracking systems for instrument localization with pure image-based 6DoF pose estimation using deep-learning methods. However, state-of-the-art single-view pose estimation methods do not yet meet the accuracy required for surgical navigation. In this context, we investigate the benefits of multi-view setups for highly accurate and occlusion-robust 6DoF pose estimation of surgical instruments and derive recommendations for an ideal camera system that addresses the challenges in the operating room.

The contributions of this work are threefold. First, we present a multi-camera capture setup consisting of static and head-mounted cameras, which allows us to study the performance of pose estimation methods under various camera configurations. Second, we publish a multi-view RGB-D video dataset of ex-vivo spine surgeries, captured in a surgical wet lab and a real operating theatre and including rich annotations for surgeon, instrument, and patient anatomy. Third, we evaluate three state-of-the-art single-view and multi-view methods for the task of 6DoF pose estimation of surgical instruments and analyze the influence of camera configurations, training data, and occlusions on the pose accuracy and generalization ability. The best method utilizes five cameras in a multi-view pose optimization and achieves an average position and orientation error of 1.01 mm and 0.89° for a surgical drill as well as 2.79 mm and 3.33° for a screwdriver under optimal conditions. Our results demonstrate that marker-less tracking of surgical instruments is becoming a feasible alternative to existing marker-based systems.

© 2023 Elsevier B. V. All rights reserved.

1. Introduction

Computer-assisted interventions have benefited significantly from advances in computer vision (Mascagni et al., 2022) to increase autonomy, accuracy, and usability for tasks such as nav-

igation, surgical robotics, surgical phase recognition, or automated performance assessment (Farshad et al., 2021; Doughty and Ghugre, 2022; Haidegger et al., 2022; Garrow et al., 2021; Lam et al., 2022). While most methods are currently being studied in isolation for specific use cases, the intention is to integrate them holistically in a new generation of operating rooms optimized for the utilization of computer vision (Feußner and Park,

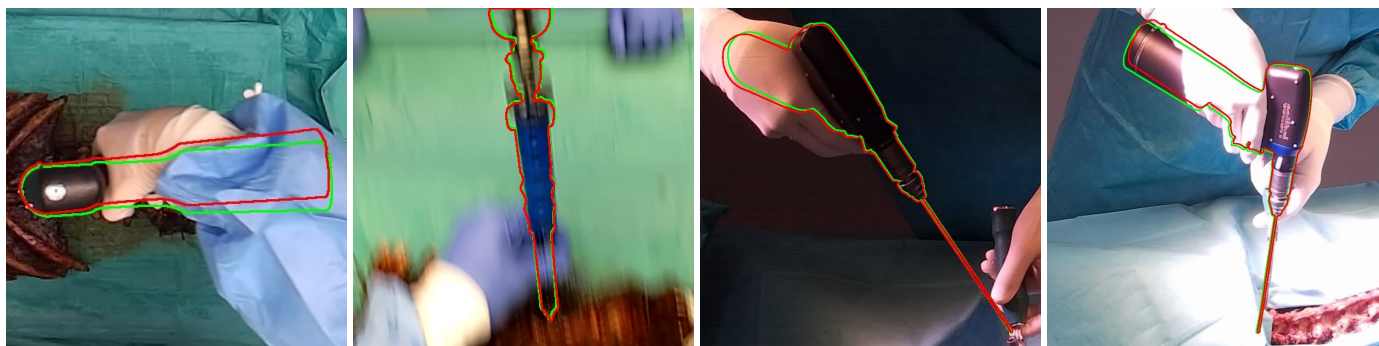


Fig. 1: Excerpt of our test set in a surgical wet lab (left) and an operating room (right). 6DoF pose estimation of surgical instruments is a complex task due to challenging lighting conditions, frequent occlusions, as well as motion blur in ego-centric perspectives. The superimposed outlines indicate the ground truth pose (green) and the pose estimate of our multi-view baseline (red).

2017; Maier-Hein *et al.*, 2022; Özsoy *et al.*, 2023). Hereby, the data streams are utilized to support the surgical staff in all relevant aspects of a surgery ranging from clinical process optimization to precision surgery (Özsoy *et al.*, 2022).

In precision surgery, a particular significance is attributed to surgical navigation, which improves the safety and efficiency of interactions between the surgeon, instruments, and the patient (Virk and Qureshi, 2019). Marker-based navigation systems have been available for over two decades and have been shown to increase accuracy and reduce revision rates (Girardi *et al.*, 1999; Luther *et al.*, 2015; Perdomo-Pantoja *et al.*, 2019). However, the restricted application range and inherent technical limitations such as line-of-sight issues, extensive calibration requirements, and the impracticality of large tracking markers complicate the integration into the existing surgical workflow, thus limiting acceptance and dissemination (Härtl *et al.*, 2013; Joskowicz and Hazan, 2016).

In recent years, several works investigated marker-less tracking approaches based on deep learning to overcome these limitations. Many of those works focus on 2DoF pose estimation of surgical instruments on the image plane (Qiu *et al.*, 2019; Zhao *et al.*, 2019), or estimate a 6DoF pose based on strong assumptions on the instrument shape (Hasan *et al.*, 2021; Chiu *et al.*, 2022) or the image appearance (Allan *et al.*, 2015), which limits generalization. Among the most recent methods, Hein *et al.* (2021) and Doughty and Ghugre (2022) estimate the 6DoF pose of a hand-held instrument from egocentric RGB-D frames by leveraging correlations between hand and instrument poses. Other works propose registration-based methods with depth sensors (Lee *et al.*, 2017), as similar approaches have been successfully applied to register the patient anatomy (Lee *et al.*, 2017; Liebmann *et al.*, 2023). However, these approaches failed to achieve a sufficient accuracy in our use case due to frequent occlusions.

As a fundamental computer vision problem, marker-less object pose estimation remains an active research focus with a continuously improving state of the art. Most proposed methods operate on single RGB frames due to the wide applicability (Hinterstoisser *et al.*, 2012; Xiang *et al.*, 2018; Wang *et al.*, 2021), however, their accuracy is limited by depth ambiguities. Other works circumvent this issue by employing RGB-D sen-

sors (Labbé *et al.*, 2020; Haugaard and Buch, 2022) or multiple views (Labbé *et al.*, 2020; Shugurov *et al.*, 2021; Haugaard and Iversen, 2023), and report high pose accuracy and occlusion-robustness. Such state-of-the-art object pose estimation methods have been successfully applied in various fields like robotic grasping (Wang *et al.*, 2019), augmented reality (Liu *et al.*, 2022), or outer space (Hu *et al.*, 2021). However, the translation of those methods to the surgical domain is largely hindered by the lack of publicly available datasets for training and evaluation (Bouget *et al.*, 2017; Mascagni *et al.*, 2022).

In the surgical domain, most existing datasets provide limited 2D annotations such as bounding boxes, tool tip positions, or segmentation masks (Sarikaya *et al.*, 2017; Allan *et al.*, 2020), preventing their use for supervised training of 6DoF pose estimation methods. Several datasets provide 6DoF pose annotations based on the Da Vinci robotic platform (Allan *et al.*, 2015; Speidel *et al.*, 2023) but are inherently focused on minimally invasive surgery only. For a few datasets, the instrument pose was recovered indirectly via the surgeon’s hand by utilizing grasp information (Hein *et al.*, 2021; Wang *et al.*, 2023). While this approach enables automated annotations from only RGB(-D) images, the accuracy of the estimated instrument pose may not be sufficient for clinical applications due to accumulating errors in the hand pose and grasp estimation. To the best of our knowledge, there is no publicly available multi-camera dataset suitable for the task of 6DoF tracking of surgical instruments to date.

In this work, we contribute a comprehensive multi-modal and multi-camera spine surgery dataset, in which operations were performed on human ex-vivo anatomy using real surgical instruments. The setup includes RGB-D video streams from a total of seven static and head-mounted cameras, as well as a marker-based tracking system with sub-millimeter accuracy to obtain highly accurate pose annotations for the instruments and head-mounted devices (HMDs). The dataset is captured in a surgical wet lab as well as in a real operating room and contains a total of 23 recordings from five different operators and two different instruments. Furthermore, we provide a comprehensive evaluation of the potential and accuracy of a custom-made 6DoF tracking system comprising multiple off-the-shelf cameras and state-of-the-art pose estimation methods. We compare

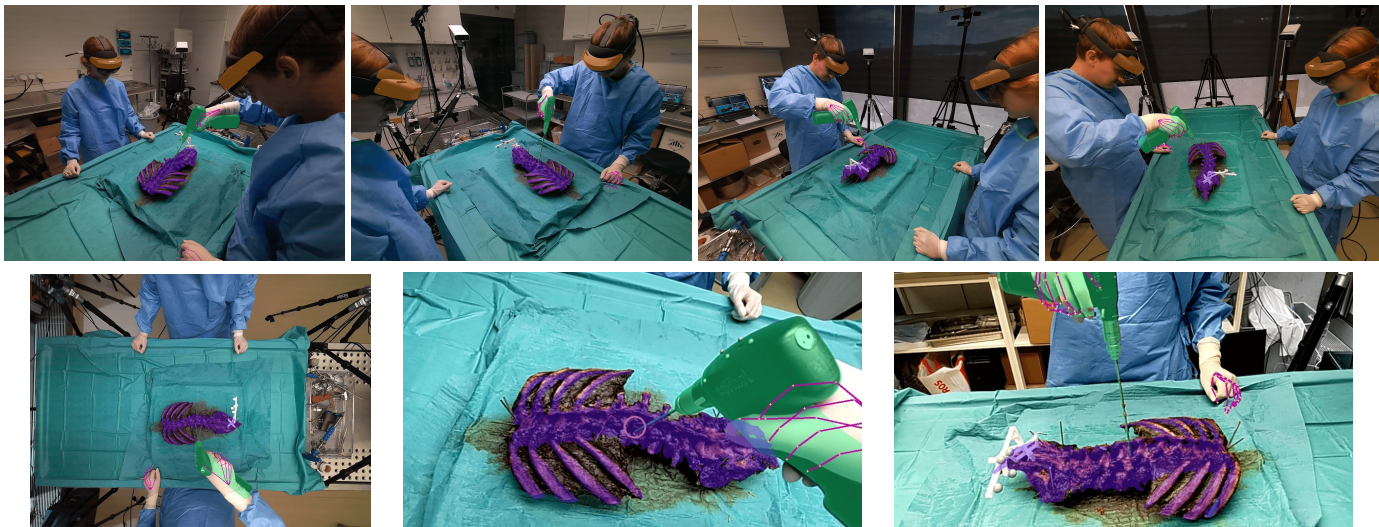


Fig. 2: Overview of the camera views in the surgical wet lab setup, with ground truth pose overlays of the drill, anatomy, hand tracking, and eye gaze. The shown cameras are (top-to-bottom, left-to-right) left (L), opposite left (OL), opposite right (OR), right (R), ceiling (C), surgeon (S), and assistant (A).

the performance of three state-of-the-art single- and multi-view pose estimation methods in the surgical domain. In this context, we evaluate the impact of the number of cameras and camera placements, the benefits of ego-centric perspectives from HMDs, as well as the performance of static, hybrid, or fully mobile camera configurations. We furthermore assess the effects of different training strategies and limited real training data on the pose accuracy, robustness to occlusions, and generalizability. We demonstrate that marker-less tracking is becoming a feasible alternative to existing marker-based navigation systems. Last, we provide additional annotations of the anatomy- and hand pose, as well as eye gaze information, which were obtained from the marker-based tracking system and the HMDs. Although these annotations are not utilized by the selected instrument pose estimation baselines, they enable further use cases of our dataset. The dataset will be publicly available on our project page <https://jonashein.github.io/mvps/>.

2. Methodology

Our 6DoF marker-less tracking approach is tailored to open surgery procedures. We selected spinal surgery as a representative use case due to its prevalence and the stringent accuracy requirements involved. Our objective is to track the 3D position and orientation of two frequently utilized surgical instruments: a surgical drill and a screwdriver.

The subsequent sections of this chapter are organized as follows: in Sections 2.1 and 2.2, we introduce the multi-camera acquisition setup as well as the joint calibration and synchronization method developed for our study. Next, we present two datasets captured in a surgical wet lab and a real operating room, which are suitable for the evaluation of pose estimation and tracking methods, as well as for the training of learning-based models. These datasets are presented in Section 2.3. Last, we describe the integration of the state-of-the-art pose estimation baselines into our tracking system in Section 2.4.

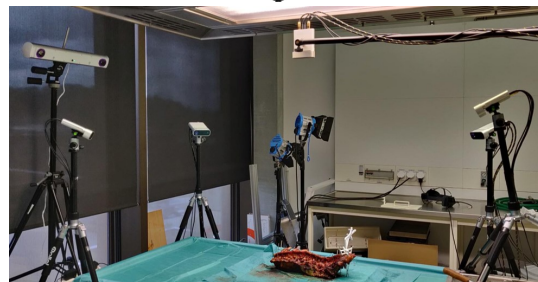
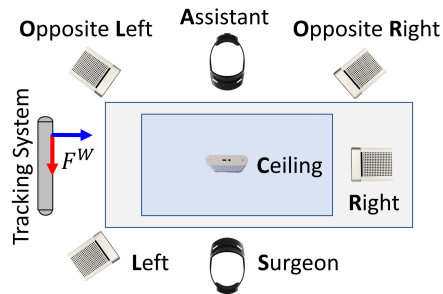


Fig. 3: Overview of the multi-camera acquisition setup in the surgical wet lab. Multiple static RGB-D cameras are placed around the operating field and on the ceiling. The surgeon and assistant are equipped with HMDs. All cameras are calibrated beforehand. To obtain accurate ground truth data, all instruments and HMDs are tracked with a marker-based tracking system.

2.1. Camera Setup

Our envisioned camera setup for a next-generation operating room (as shown in Figures 2 and 3) consists of multiple static and mobile cameras, the latter in the form of augmented reality HMDs that are worn by the surgeons. We place four Azure Kinect cameras (Microsoft Corporation, Redmond, WA, USA) around the surgical site, while a fifth Azure Kinect camera captures a bird-eye-view of the operating table, similar to the perspective of a camera integrated into overhead OR lights. In addition, two HoloLens 2 (HL 2, Microsoft Corporation, Redmond, WA, USA) devices capture the egocentric perspectives of the operating surgeon and an assistant, and provide hand pose

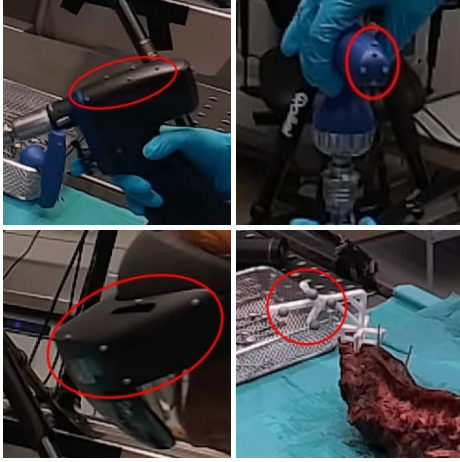


Fig. 4: Both instruments, the HMDs, and the anatomy are tracked with a marker-based tracking system. We use hemispherical fiducials with 3 mm diameter on instruments and HMDs, and spherical fiducials with 12 mm diameter for the anatomy.

and eye gaze information.

Ground Truth Generation. In addition to the aforementioned cameras, we track the surgical instruments and HL 2 devices using a FusionTrack 500 marker-based tracking system (Atracsys LLC, Puidoux, Switzerland) to obtain accurate ground truth pose annotations and to circumvent potential errors of the HL 2 integrated SLAM system. As shown in Figure 4, we place small infrared (IR) reflective hemispheres with a diameter of 3 mm on the object surfaces to minimize appearance changes. To calibrate the attached IR marker arrays we acquire 3D models of all instruments and the HoloLenses using a high-fidelity 3D scanner (Artec3D, Senningerberg, Luxembourg).

Besides the instruments, we also track the anatomy via an IR marker array attached to the sacrum. To this end, a post-experimental CT scan was acquired, from which 3D models of the spine anatomy were created by segmentation (Mimics Medical, Materialise NV, Leuven, Belgium). We used the method proposed by Liebmann *et al.* (2021) to register all 3D models to their attached marker coordinate frames. Although the anatomy pose is not relevant to evaluate instrument pose estimation models, it enables further uses of our dataset as discussed in Section 4.1.

2.2. Camera Calibration and Temporal Synchronization

An accurate calibration of camera extrinsic and synchronization parameters is crucial when collecting a multi-camera dataset. To give an intuition, a synchronization error of 8 ms between the devices will result in a position error of 2 mm for a surgical instrument moving with a speed of 0.25 m/s relative to the camera. We found the synchronization via the host computer’s real-time clock to be insufficient due to varying latencies of the devices. Instead, we jointly optimize extrinsic and synchronization parameters by minimizing the average re-projection error of a moving multi-modal marker B that can be recognized by the tracking system W , the HMDs P_i and static cameras K_j at the beginning of every recording. Hereby, we

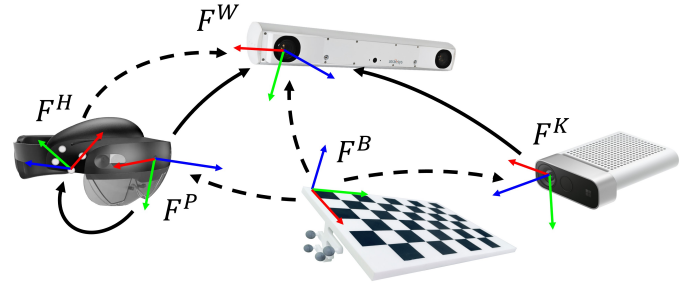


Fig. 5: Schematic overview of the coordinate frames and transformations used for the joint extrinsic calibration and synchronization. Indicated are relevant transformations between the coordinate frames of the calibration board F^B , the tracking system F^W , a stationary camera F^K , a HMD camera F^P and the attached IR marker array F^H . Dashed lines indicate that the transformation is estimated via PnP.

directly estimate the offset between all device-internal clocks, using the tracking system W as a reference. Similarly, we define the tracking system W as the world coordinate frame F^W and co-register all cameras F_i^P and F_j^K with this reference frame using a self-designed multi-modal calibration board F^B similar to the work by Liebmann *et al.* (2021). A schematic overview of the calibrated transformations is shown in Figure 5. The extrinsic calibration of static and mobile cameras in our setup differs slightly due to the outside-in tracking of the HMDs, so we provide both variants in the next paragraphs. Note that we calibrate the intrinsic parameters of all cameras in a separate step prior to the extrinsic calibration and synchronization using the method by Zhang (2000). In the following, we denote a transformation from coordinate frame F^A to frame F^B as T_{A}^B , and omit the indices for cameras P_i and K_j to improve readability.

To spatio-temporally register a static camera K with the reference tracking system W , we observe a sequence

$$\{(x_i^K, t_i^K) \mid 1 \leq i \leq N\} \quad (1)$$

of 2D marker locations x_i^K and timestamps t_i^K from camera K , and a sequence

$$\{(T_{B,m}^W, t_m^W) \mid 1 \leq m \leq M\} \quad (2)$$

of 6D marker poses $T_{B,m}^W$ and timestamps t_m^W from the reference system W . We piece-wise linearly interpolate the pose sequence, obtaining the function $f_B^W : t_m \rightarrow T_{B,m}^W$. Then, the camera’s extrinsic parameters T_W^K and synchronization parameters δt^K can be estimated by minimizing the re-projection error over the entire sequence

$$T_W^K, \delta t^K = \operatorname{argmin}_{T_W^K, \delta t} \sum_{1 \leq i \leq N} \|\pi_K(\hat{T}_W^K f_B^W(t_i^K + \delta t) X_i) - x_i^K\|_2, \quad (3)$$

where π_K is the projection onto the image plane of camera K and X_i are the 3D marker points in their local coordinate frame F^B .

Similarly, for a HMD P we observe the sequences

$$\{(x_i^P, t_i^P) \mid 1 \leq i \leq N\} \quad (4)$$

of 2D marker locations x_i^P and timestamps t_i^P , and

$$\{(T_{B,m}^W, t_m^W) \mid 1 \leq m \leq M\} \quad (5)$$

of 6D marker poses $T_{B,m}^W$ and timestamps t_m^W from the reference system W . Since each HMD P is tracked outside-in, we additionally observe a sequence

$$\{(T_{H,k}^W, t_k^W) \mid 1 \leq k \leq K\} \quad (6)$$

of 6D HMD marker poses $T_{H,k}^W$ and timestamps t_k^W from the tracking system W , which we piece-wise linearly interpolate to obtain the function $f_H^W : t_k \rightarrow T_{H,k}^W$. Then, the temporal offset δt^P can be estimated by minimizing the re-projection error over the entire sequence

$$\delta t^P = \underset{\delta t}{\operatorname{argmin}} \sum_{1 \leq i \leq N} \|\pi_P(T_H^P f_H^W(t_i^P + \delta t)^{-1} f_B^W(t_i^P + \delta t) X_i) - x_i^P\|_2, \quad (7)$$

where π_P is the projection onto the image plane of camera P , and T_H^P is the transformation between the HMDs camera sensor F^P and the attached marker array F^H , which is calibrated separately beforehand. Note that the optimization objective can be generalized to mobile cameras with inside-out tracking, however, we decided to use the more accurate outside-in tracking to minimize this source of error in the evaluations.

Both objectives are optimized using LO-RANSAC (Chum *et al.*, 2003) with an inlier threshold of $\theta = 2\text{px}$ and the Levenberg-Marquardt algorithm. Due to the limited temporal resolution of the sequences, we locally optimize the temporal offset via a grid search with a step size of $250\mu\text{s}$. Note that since the Azure Kinect supports hardware synchronization, we only optimize the time shift δt^K of the first device and keep it fixed for all remaining ones.

Ground Truth Quality. We evaluate the accuracy of the camera extrinsic calibration and synchronization by comparing the calibration board corner locations as detected in the camera images with their corresponding ground truth positions. The average re-projection error is 1.82px , which corresponds to mean errors of 0.88mm and 0.83mm along the camera's X and Y axes, respectively. Note that these errors include both spatial and temporal calibration errors as they refer to a moving target.

2.3. Surgery Datasets

Surgical Wet lab. To evaluate our approach, we record the instrumentation phase of spinal fusion surgery using the presented multi-camera acquisition setup in a surgical wet lab. Spinal instrumentation consists of pre-drilling a screw trajectory, implantation, and removal of a pedicle screw implant. Hereby, we use a Colibri II battery-powered drill (DePuy Synthes, Raynham, MA, USA) for pre-drilling, and a polyaxial pedicle screwdriver (Medacta SA, Castel San Pietro, Switzerland) for screw insertion. Both instruments are subject to our marker-less pose estimation system. Screw implantation is conducted on three human specimens between T10 and L5 vertebrae by one trained surgeon and three researchers using pre-drilled optimal screw trajectories.

The static cameras capture RGB frames with a resolution of 2048×1536 pixels and 30 frames per second (fps). Both HMDs capture RGB frames with a resolution of 896×504 pixels and 30 fps, though the effective frame rate is lower due to frequently dropped frames. The dataset contains a total of 21 recordings with 1.7M frames. Each recording consists of a varying number of pre-drilling, screw implantation, and removal steps, in random order. Also, the scrubs and glove colors are randomized to increase the image diversity.

We split the dataset into 17 training recordings and 4 test recordings. From the 4 test recordings we sample 6223 multi-view image sets with 7 camera views each, for a total of 43561 RGB-D frames. In the sampling process, we ensure that the pair-wise temporal offset between RGB exposure windows within each multi-view set is at most 8ms. This filtering step is necessary because we can only synchronize the device-internal clocks but not the camera shutters. In contrast to the Azure Kinect, neither the HL 2 nor the FusionTrack 500 support any hardware-synchronization of the photo-video (PV) camera shutter, e.g. with an external trigger signal. As such, there will be varying temporal offsets of up to 16.7ms between pairs of captured images from multiple cameras (assuming 30fps). These temporal offsets break the underlying assumptions of multi-view pose estimation models and may introduce additional errors depending on the dynamics in the scene. We evaluate the effect of this temporal offset in the appendix but find no significant correlation between the temporal offset of image pairs and the accuracy of the multi-view pose estimates in our experiments.

Synthetic Dataset. In addition to the real images, we render synthetic images of the instruments to support the training process (Movshovitz-Attias *et al.*, 2016). We generate 25k renderings from uniformly sampled poses with a distance between 0.4m to 1.7m, matching the distance range of the wet lab dataset. Additionally, we generate 38k photo-realistic renderings using BlenderProc2 with the same sampling strategy (Denninger *et al.*, 2023). The synthetic images do not include the anatomy but show random textures from the CC0 texture library¹ or a black background. Note that all synthetic renderings show the instruments in the same articulation and without any IR markers.

OR-X Test Set. To show that our system can be translated to a realistic environment, we additionally capture a second test set in the OR-X², a real operating theatre dedicated to research use. This test set consists of five Azure Kinect cameras attached to the ceiling around the operating table, as illustrated in Figure 7. All cameras are mounted above head height to minimize the invasiveness of our setup. We collect two subsets totaling about 25k frames, where each subset consists of one recording of pedicle screw pre-drilling with the Colibri II³. In both

¹<https://ambientcg.com/>

²<https://or-x.ch/>

³For logistic reasons the OR-X test set does not include tracked anatomy or the pedicle screwdriver. HMDs were excluded due to their poor performance on preliminary experiments.

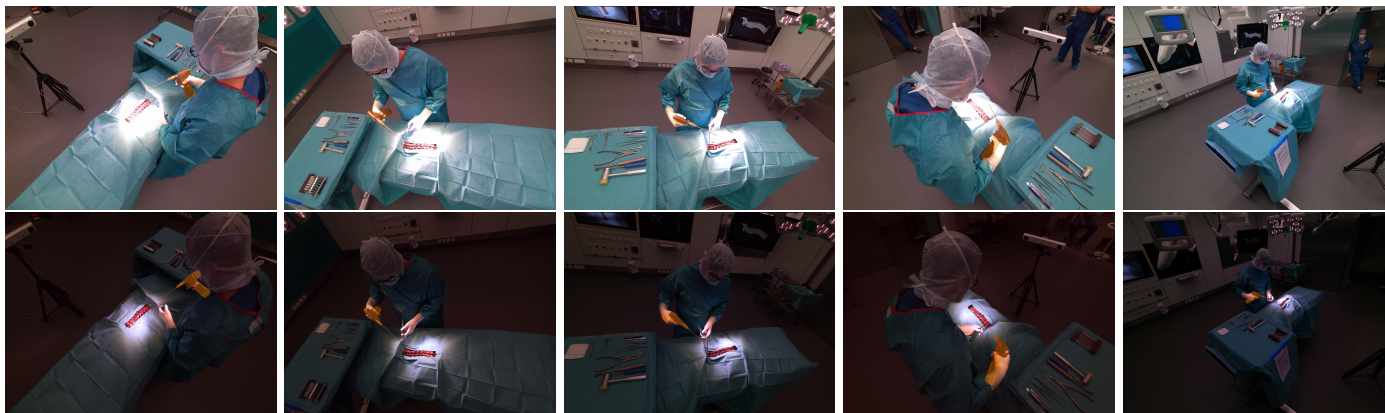


Fig. 6: Comparison of the camera views and exposure windows used in the OR-X test set, with the multi-view pose estimates of EpiSurfEmb superimposed. The shown cameras are (left-to-right) left (L), opposite left (OL), opposite right (OR), right (R), and far (F). The first recording (top row) was captured with a longer exposure time that is optimal for acquiring the entire surgery room environment, but results in an overexposed surgical near field. The second recording (bottom row) was captured with a shorter exposure time optimal for the surgical near field, but the environment is generally underexposed.

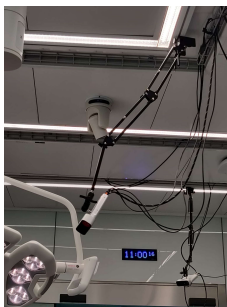
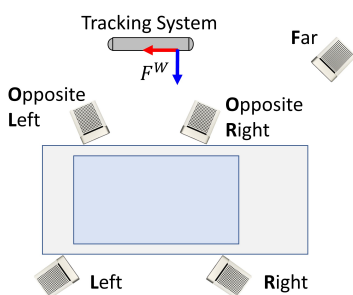


Fig. 7: Schematic overview of the camera setup for the OR-X test set (left) and an exemplary ceiling-mounted camera in the OR-X (right).

subsets, the drill is operated by a surgeon in training. The calibration, synchronization, and data processing are carried out identically to the generation of the training dataset.

Besides the more realistic environment, the OR-X test set has additional and intentional differences compared to the wet lab dataset which enables the evaluation of the model’s robustness and generalizability. First, both subsets were captured with different exposure settings to obtain significantly differing and more challenging lighting conditions. Second, camera-to-camera and camera-to-instrument distances are significantly larger compared to the wet lab setup with cameras rigidly fixed on arms attached to the ceiling. To compensate for the increased distance range of about 0.9 m to 2.8 m, we record this test set in 4K resolution instead of 1536p. Third, the drilling in the OR-X test set is conducted with the help of a drill sleeve, which is not used in the wet lab dataset. Exemplary frames can be seen in Figure 6.

This test dataset is used exclusively to analyze the robustness and generalizability of models to novel environments. As such, it is not used for training or refinement in any experiment.

2.4. Pose Estimation Baselines

We select Zebrapose (Su et al., 2022) and Surfemb (Haugaard and Buch, 2022) as our single-view baselines, and

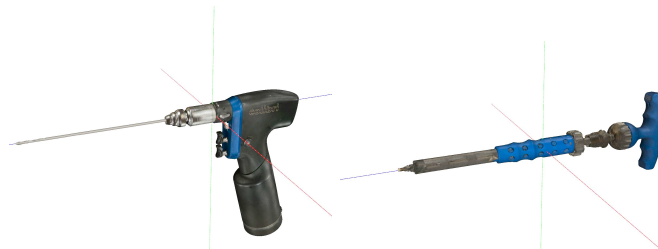


Fig. 8: Local coordinate frames of the tracked surgical drill (left) and screwdriver (right).

EpiSurfEmb (Haugaard and Iversen, 2023) as our multi-view baseline. This selection is motivated by their state-of-the-art performance on the benchmark for 6D object pose estimation (BOP) (Hodan et al., 2018). Other multi-view pose estimation methods like Cosypose (Labbé et al., 2020) and DPODv2 (Shugurov et al., 2021) were discarded as they are either not designed for multi-view single-object pose estimation or do not provide a reference implementation. Also, in contrast to end-to-end trained pose estimation models, the selected baselines estimate 2D-3D correspondences as an intermediate representation and recover the 6DoF pose by solving an interpretable geometric optimization problem. The interpretability of this intermediate representation can be utilized to compute the uncertainty of the pose estimate in the future (Haugaard et al., 2023), which is highly relevant to avoid presenting inaccurate information to the surgeon.

Zebrapose (Su et al., 2022) iteratively divides the target object’s surface into two equal parts in N hierarchical steps. The entire surface is thus divided into 2^N fragments, whereby each fragment can be identified with a binary code of length N . The bits of the binary code effectively describe 2D-3D correspondences with increasing granularity. A model $f : \mathbb{R}^{H \times W \times 3} \rightarrow \mathbb{R}^{H \times W \times N+1}$ is trained to estimate the mask and per-pixel binary code of the $H \times W$ sized RGB image. During training, the loss for each bit is gradually adjusted to shift the focus from coarse to fine correspondences. The 6DoF pose estimate is computed

using progressive-x (Barath and Matas, 2019).

Similar to Zebrapose, SurfEmb (Haugaard and Buch, 2022) estimates 2D-3D correspondences via intermediate descriptors for the 3D surface. However, the authors propose to learn a surface embedding instead of using hand-crafted descriptors. A key model $g : \mathbb{R}^3 \rightarrow \mathbb{R}^E$ maps 3D points on the object’s surface to keys in a latent space \mathbb{R}^E . A query model $f : \mathbb{R}^{H \times W \times 3} \rightarrow \mathbb{R}^{H \times W \times E+1}$ estimates the object mask as well as a per-pixel query based on the RGB input, where keys and queries live in the same latent space \mathbb{R}^E . Pose hypotheses are sampled from the 2D-3D correspondence distribution via RANSAC-PnP with an inlier threshold of $\theta = 2\text{px}$ and scored based on the agreement of object mask and correspondence distributions under the pose hypothesis. The best pose hypothesis is locally optimized based on the correspondences and optionally refined on the range map obtained from a depth sensor, if available.

EpiSurfEmb (Haugaard and Iversen, 2023) extends SurfEmb to multi-view input. Given a set of input images and the relative camera poses, EpiSurfEmb estimates a 3D-3D correspondence distribution based on the per-view 2D-3D correspondence distributions obtained from SurfEmb. Hereby, 3D points are triangulated from pairs of corresponding 2D points in two randomly selected views, taking into account epipolar constraints. Pose hypotheses are sampled from the 3D-3D correspondence distribution via RANSAC and Kabsch’s algorithm.

3. Results

Based on the selected baseline models, we evaluated the effect of several parameters on the pose accuracy, namely the number of cameras, their spatial configuration, and the size of the real training dataset. All experiments are conducted on cropped image patches based on the ground truth 2D bounding box. In practice, these image patches can be obtained using a 2D bounding box detector or - in a tracking approach - via the estimated pose on the previous frame (Redmon and Farhadi, 2018; Fang *et al.*, 2021). For each baseline, we train a single model to estimate the poses of both instruments. Given that EpiSurfEmb is built upon SurfEmb, the key and query models are trained only once and then used for both single-view and multi-view assessments.

Throughout this section and concerning the parameters above, we compare three different training strategies, namely using only synthetic data, only real data, or training jointly on both synthetic and real data. For the joint training on both data types, each model was first trained exclusively on the synthetic dataset until convergence, and then refined on both synthetic and real data of the wet lab dataset. All models were trained with a cyclic learning rate between 1×10^{-4} to 1×10^{-5} , which was determined via a range test as proposed by Smith (2018). We show in Section 3.3 that the models trained jointly on synthetic and real data show the best generalization abilities. Unless otherwise specified, models were trained using this strategy.

Evaluation Metrics. Following Hinterstoisser *et al.* (2012) we evaluate the performance of all models using the ADD(-S) metric, which measures the average distance between correspond-

ing object vertices under the estimated and the ground truth pose. For symmetric objects like the screwdriver, the metric corresponds to the average distance to the closest vertex under the ground truth pose. We additionally report the position error of the instrument origin and the orientation error, as depicted in Figure 8. Last, we evaluate the pose accuracy relative to the commonly used visibility factor (Hodan *et al.*, 2018), which is defined as the area of the modal mask relative to the area of the amodal mask.

3.1. Camera Configurations and Pose Estimation Accuracy

To find the optimal camera configuration, we exhaustively evaluate the baselines across all possible 127 camera configurations, ranging from 1 to 7 cameras, as depicted in Figure 3. The results of our single- and multi-view pose estimation baselines are summarized in Table 1.

EpiSurfEmb trained on purely real data achieves the highest pose accuracy with average ADD(-S) errors of 1.85 ± 1.10 mm and 1.42 ± 1.44 mm for drill and screwdriver, respectively, using five static cameras. The mean position and orientation errors for the drill are 1.01 mm and 0.89° , while we observe errors of 2.79 mm and 3.33° for the screwdriver. However, as we discuss in Section 3.3, models trained jointly on synthetic and real data show significantly better generalization capabilities, which is required to achieve sufficient robustness for clinical applications. We focus on these models in the following evaluations.

On single-view RGB patches, Zebrapose and SurfEmb achieve a similar pose accuracy of about 12.5 mm average ADD error for the drill. In comparison, the pose estimates for the screwdriver are less accurate, with about 2 - 4 times larger position and orientation errors. Also, SurfEmb significantly outperforms Zebrapose on the screwdriver. As shown in Figure 9, we further observe slight performance differences between the static cameras. The best single view is provided by the opposite right camera, where SurfEmb achieves the lowest average ADD(-S) error of 6.85 mm. Pose estimates based on the surgeon’s perspective are significantly less accurate on average, which is due to the narrow field of view (FOV) and the proximity to the instruments, resulting in frequent and heavy truncation.

The depth refinement step proposed by Haugaard and Buch (2022) does not consistently improve the pose accuracy, but can significantly degrade it. We found that this degrading performance is mainly caused by a lack of robustness against partial occlusions, as well as limitations of the depth sensor. Similarly, we observe that the ICP refinement proposed for Zebrapose severely decreases the average pose accuracy. These results are in line with our preliminary evaluations of ICP on the captured point clouds, where the average pose error was about 7 mm even when initializing ICP with the ground truth pose. We include representative failure cases in the appendix.

To evaluate the influence of occlusions on the pose accuracy, we evaluate the visibility distributions for all cameras and express the mean ADD(-S) error (prior to depth refinement) as a function of the relative visibility. The results are shown in Figure 10. The average instrument surface visibility from the surgeon’s perspective is only 19%, which is significantly lower

Table 1: We report the ADD(-S), position, and orientation errors of the single-view RGB(-D) and multi-view RGB baselines as mean \pm std. The orientation error ΔR is defined as the geodesic distance between the estimated and ground truth rotation. Bold and underlined font indicates the lowest and second-lowest average error, respectively. Single-view results are averaged over all cameras. Both single-view baselines estimated a few ($< 0.7\%$) unrealistic poses with > 1 m position errors, which were excluded from the evaluation. The camera identifiers are opposite left (OL), opposite right (OR), ceiling (C), left (L), right (R), surgeon (S), and assistant (A), as shown in Figure 3. * indicates hybrid camera setups with static and mobile cameras. † indicates fully mobile camera configurations.

Model	Drill			Screwdriver		
	ADD (mm) ↓	Δt (mm) ↓	ΔR (deg) ↓	ADD-S (mm) ↓	Δt (mm) ↓	ΔR (deg) ↓
ZebraPose	12.57 \pm 29.19	11.13 \pm 32.35	3.69 \pm 12.03	22.58 \pm 44.15	41.44 \pm 88.10	15.75 \pm 21.76
ZebraPose + ICP	48.58 \pm 62.88	47.38 \pm 76.64	21.05 \pm 26.23	17.16 \pm 33.75	37.77 \pm 82.81	25.17 \pm 26.64
SurfEmb	12.46 \pm 21.64	11.04 \pm 27.16	3.37 \pm 6.66	12.70 \pm 25.33	25.65 \pm 56.37	12.98 \pm 17.23
SurfEmb RGB-D	20.80 \pm 41.95	24.59 \pm 68.40	3.40 \pm 6.98	11.80 \pm 22.23	24.75 \pm 53.73	13.05 \pm 17.40
EpiSurfEmb (multi-view, trained on synthetic and real data)						
OL+OR	2.26 \pm 1.25	1.34 \pm 0.83	1.08 \pm 0.69	1.73 \pm 1.60	3.29 \pm 3.22	5.37 \pm 5.14
L+OL+OR+R	<u>2.02 \pm 1.16</u>	1.15 \pm 0.73	1.00 \pm 0.62	1.53 \pm 1.46	<u>2.91 \pm 2.81</u>	4.77 \pm 4.10
L+OL+OR+R+C	2.02 \pm 1.22	<u>1.06 \pm 0.71</u>	<u>0.95 \pm 0.61</u>	<u>1.47 \pm 1.44</u>	<u>2.95 \pm 2.82</u>	3.29 \pm 2.65
L+OL+OR+R+C+S+A*	2.14 \pm 1.22	1.22 \pm 0.81	1.00 \pm 0.60	1.52 \pm 1.44	3.11 \pm 2.83	3.48 \pm 2.82
L+C	3.56 \pm 2.99	2.13 \pm 1.48	1.56 \pm 1.63	2.09 \pm 2.05	4.59 \pm 4.36	4.00 \pm 5.66
R+A*	4.20 \pm 2.48	3.35 \pm 2.59	1.66 \pm 1.11	2.47 \pm 1.90	5.17 \pm 4.20	7.44 \pm 7.35
R+S*	6.35 \pm 7.65	5.79 \pm 7.58	2.49 \pm 2.18	7.38 \pm 8.51	15.53 \pm 15.62	9.20 \pm 8.83
R+S+A*	3.95 \pm 2.07	3.13 \pm 2.12	1.79 \pm 1.07	2.31 \pm 1.75	4.70 \pm 3.60	7.58 \pm 7.51
S+A†	9.50 \pm 11.28	7.45 \pm 9.49	3.82 \pm 5.89	7.08 \pm 12.29	12.60 \pm 15.65	17.65 \pm 17.62
EpiSurfEmb (multi-view, trained purely on synthetic data)						
OL+OR	7.80 \pm 6.74	3.38 \pm 2.96	3.81 \pm 4.20	3.60 \pm 2.38	6.59 \pm 4.50	14.06 \pm 15.39
L+OL+OR+R+C	5.19 \pm 3.02	2.41 \pm 1.13	2.46 \pm 1.64	2.42 \pm 3.19	4.48 \pm 4.35	7.33 \pm 9.65
EpiSurfEmb (multi-view, trained purely on real data)						
OL+OR	2.26 \pm 1.26	1.42 \pm 1.01	1.06 \pm 0.68	1.60 \pm 1.58	3.07 \pm 3.07	4.91 \pm 4.96
L+OL+OR+R+C	1.85 \pm 1.10	1.01 \pm 0.70	0.89 \pm 0.58	1.42 \pm 1.44	2.79 \pm 2.81	<u>3.33 \pm 2.68</u>

than the average visibility of 63% for all other cameras. We find that a relative visibility of less than 60% results in an exponential increase in ADD(-S) error, whereas greater visibility has little influence on the average pose accuracy. The mean ADD(-S) error on frames with at least 60% visibility is similar for all cameras and between 5.93 mm for the surgeon HMD and 8.86 mm for the left camera. On frames with a medium occlusion level between 20% to 60% the surgeon HMD is slightly outperformed by the opposite right camera with ADD(-S) errors of 8.88 mm and 8.76 mm, respectively. Nevertheless, SurfEmb achieves a low visible surface discrepancy even for heavily occluded or truncated instruments, as shown in Figure 11. We observe that approximately 90% of the position errors are along the camera’s depth (Z) axes.

In the multi-view setting, we observe consistently low average pose errors throughout all combinations of static cameras. The best configuration consists of all five static cameras and achieves an ADD(-S) error of 1.75 ± 1.33 mm. The mean position and orientation errors of the drill are 1.06 ± 0.71 mm and $0.95 \pm 0.75^\circ$. Similar to the single-view scenario, the mean position and orientation errors of the screwdriver are higher at 2.95 ± 2.82 mm and $3.29 \pm 2.65^\circ$. The worst fully-static configuration consisting of the left and ceiling cameras still achieves an ADD(-S) error of 2.83 ± 2.52 mm, which is a 60% error reduction compared to the best single-view result.

As expected, the average pose error decreases with an increasing number of cameras, as shown in Figure 12. Moreover, the best 2-view configuration consisting of the opposite left and opposite right cameras achieves an ADD(-S) error of

1.99 ± 1.42 mm, which is only 0.24 mm worse than the best configuration with five cameras. This suggests that adding viewpoints to a pair of unoccluded and complementing viewpoints leads to negligible improvements when using EpiSurfEmb with the proposed multi-camera acquisition system.

Hybrid camera configurations including the surgeon’s or assistant’s HMDs perform worse than comparable static camera configurations. Also, the addition of any HMD to the best-performing configuration of five static cameras results in a slight performance decrease. The reason may be a less accurate ground truth due to errors accumulating through the tracking of the HMDs. Nevertheless, both HMDs can improve the performance of small configurations with only two static cameras. The best hybrid 2-view configuration consists of the right static camera and the assistant’s HMD, which achieves a mean ADD(-S) error of 3.33 ± 2.19 mm.

3.2. Training Strategy

Collecting real data with accurate annotations is time-consuming and challenging, thus being able to train models on synthetic data is clearly favorable. We evaluate the SurfEmb and EpiSurfEmb on the wet lab test set after training with only a fraction of the wet lab training set, as well as after training on purely synthetic data. As can be seen in Figure 13, there is a negligible performance drop when performing the training with 1% (about 12 k) of the total real training samples instead of 100%, for both single-view and multi-view settings. Below 1% of the total real samples, the accuracy decreases significantly. Training without any real data increases the ADD(-S) error by

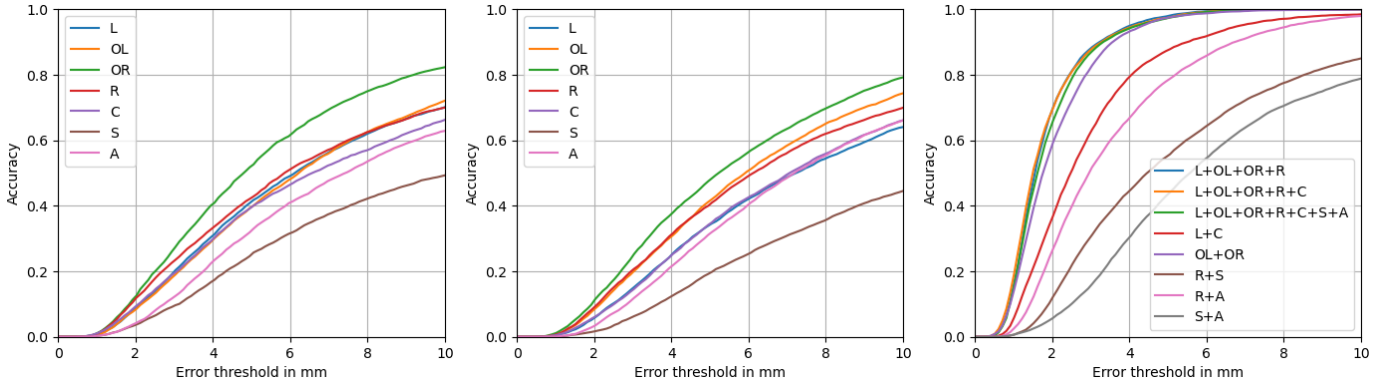


Fig. 9: Accuracy-threshold curves of the ADD(-S) error for ZebraPose (left), SurfEmb (middle), and EpiSurfEmb (right), per camera. Results are averaged over both instruments.

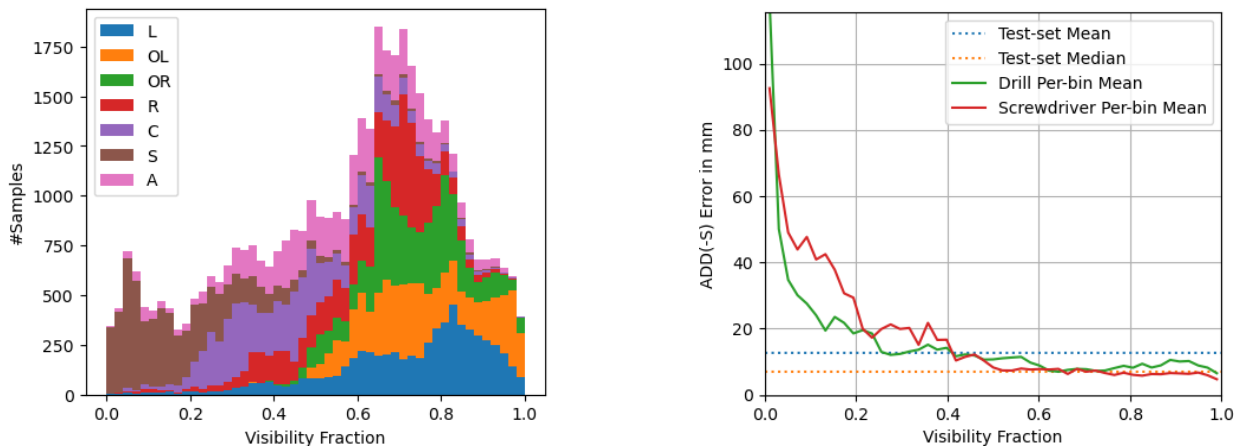


Fig. 10: The left plot shows the stacked, per-camera histograms of the visibility fractions in the wet lab dataset. The majority of frames captured with the surgeon’s HMD have a relative visibility of less than 0.2. On the right, we compare the relative visibility to the ADD(-S) error of the SurfEmb baseline, prior to depth refinement. The shown ADD(-S) error is averaged within 50 bins of equal width. We observe that the ADD(-S) error increases exponentially with decreasing visibility.

3.95 mm on average in a multi-view setting with five static cameras.

3.3. Generalizability

To estimate the generalizability to different environments we evaluate SurfEmb and EpiSurfEmb without any additional refinement on the OR-X test set and report the results in Table 2. Further qualitative results are available in the appendix.

On the bright subset, EpiSurfEmb achieves an average ADD error of 5.53 ± 5.03 mm using all five static cameras, and 6.26 ± 4.96 mm using only the opposite left and opposite right cameras. As shown in Figure 14, training solely on synthetic data results in a slightly better performance than training on both synthetic and real data, which in turn outperforms training solely on real data. These performance differences indicate that training on real data biases the model towards specific characteristics of this dataset (Torralla and Efros, 2011; Tommasi *et al.*, 2017), such as lighting conditions, the instrument pose distributions, and instrument-to-camera distances. Training without synthetic data further decreases the test-time performance, likely due to the lack of uniformly sampled viewpoints. In contrast, training exclusively on synthetic data results in a

similar performance of about 5.20 mm ADD error on the wet lab test set and the OR-X bright test subset. These results highlight the need for synthetic training data with controllable and diverse data distributions to obtain robust models.

On the dark test subset, we observe a slight performance decrease in the models trained jointly on synthetic and real, as well as solely on real data, which is to be expected due to the lack of such dark and high-contrast images in the training data. Training solely on synthetic data results in a significantly larger performance drop of 12.87 mm to 19.16 mm average ADD error on the dark subset, as well as a significantly increased variance which suggests a larger synth-real domain gap.

These results suggest that the method trained on both synthetic and real data is more robust compared to training on only one data type, and should therefore be the preferred strategy when the test environment settings, e.g. lighting conditions, camera poses, and -configurations, are unknown.

4. Discussion

Accurate tracking of surgical instruments can improve the safety and efficiency of surgical procedures. In this work,

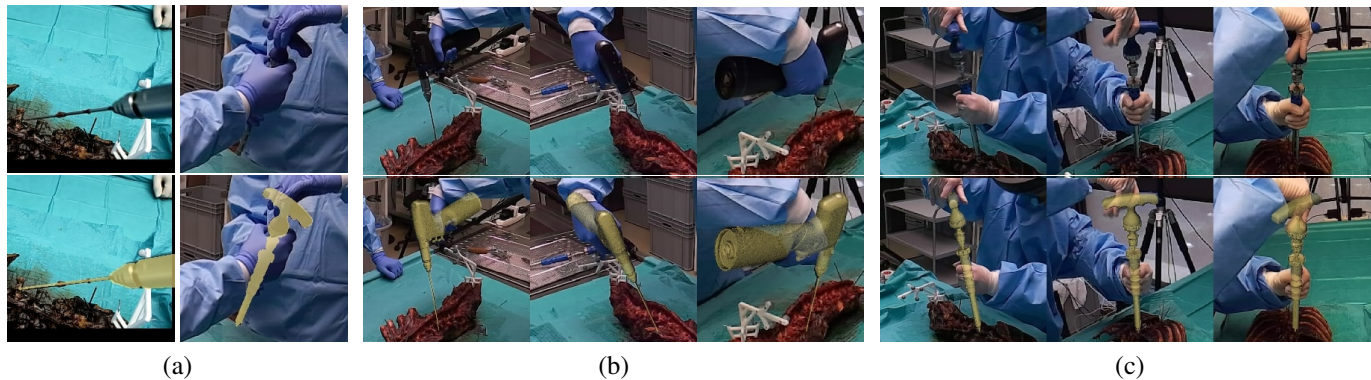


Fig. 11: Qualitative results for single-view (a) and multi-view (b) & (c). SurfEmb is robust to heavy truncations and occlusions, as shown in (a). For EpiSurfEmb three of five input views are displayed. Input RGB patches are shown in the top row. The estimated poses are superimposed in the bottom row.

Table 2: We report the ADD(-S), position, and orientation errors on the OR-X test set as mean \pm std. The orientation error is defined as the geodesic distance between the estimated and ground truth rotation. Bold and underlined font indicates the lowest and second-lowest average error, respectively. The camera identifiers as shown in Figure 7 are opposite left (OL), opposite right (OR), left (L), right (R), and far (F).

Model	Bright Subset			Dark Subset		
	ADD (mm) \downarrow	Δt (mm) \downarrow	ΔR (deg) \downarrow	ADD (mm) \downarrow	Δt (mm) \downarrow	ΔR (deg) \downarrow
EpiSurfEmb (multi-view)						
OL+OR	6.26 \pm 4.96	5.24 \pm 4.61	2.18 \pm 1.48	<u>7.79 \pm 3.51</u>	<u>6.17 \pm 3.78</u>	<u>3.13 \pm 1.73</u>
L+OL+OR+R+F	5.53 \pm 5.03	4.77 \pm 4.55	1.69 \pm 1.33	6.21 \pm 3.56	5.66 \pm 3.37	2.25 \pm 1.37
EpiSurfEmb (multi-view, trained purely on synthetic data)						
OL+OR	<u>5.46 \pm 5.26</u>	<u>4.92 \pm 4.69</u>	<u>1.60 \pm 1.44</u>	18.33 \pm 39.90	14.87 \pm 35.29	5.91 \pm 9.68
L+OL+OR+R+F	5.20 \pm 7.33	5.12 \pm 22.84	1.50 \pm 3.76	24.36 \pm 55.76	31.38 \pm 86.64	14.55 \pm 38.90
EpiSurfEmb (multi-view, trained purely on real data)						
OL+OR	7.12 \pm 5.05	6.35 \pm 4.80	2.62 \pm 1.66	9.93 \pm 5.53	8.00 \pm 4.33	4.80 \pm 3.86
L+OL+OR+R+F	6.15 \pm 4.98	5.51 \pm 4.59	1.99 \pm 1.37	7.98 \pm 3.69	7.31 \pm 3.89	3.15 \pm 1.68

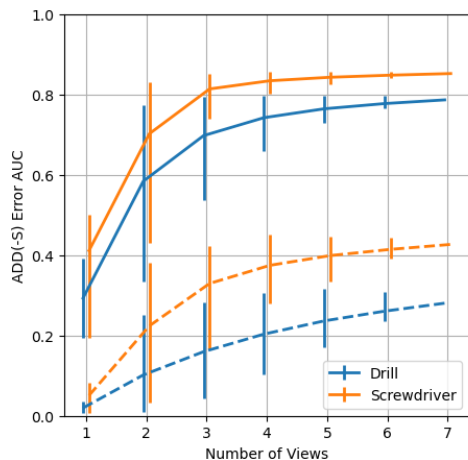


Fig. 12: Influence of the number of cameras on the area under the ADD(-S) curve (AUC) on the interval of 0 mm to 10 mm (solid lines) and on the interval of 0 mm to 2.5 mm (dashed lines). Error bars indicate the best and worst camera configuration, respectively.

we presented a multi-camera acquisition setup consisting of both static cameras and HMDs and collected a large-scale dataset with rich annotations including instrument-, anatomy- and HMD poses, as well as hands and eye gaze information. We evaluated single- and multi-camera configurations using state-of-the-art pose estimation methods to find an optimal configura-

tion serving surgical needs with respect to accuracy, occlusion, and simplicity.

Our evaluations show that monocular pose estimation methods do not satisfy the high accuracy requirements of clinical applications due to inherent depth ambiguities. These results are in line with the findings of Doughty and Ghugre (2022) and Hein *et al.* (2021), who report ADD errors of 11.71 mm and 16.73 mm for the same surgical drill in a similar setting. Our preliminary experiments showed that pose refinement on depth information obtained from time-of-flight sensors results in worse pose estimates on average. This is primarily attributed to a lacking robustness of the methods against partial occlusions, as well as a low accuracy exhibited by depth sensors. The use of RGB cameras without depth sensors brings a desirable flexibility to camera hardware and enlarges the application fields. We found that our selected pose estimation method is robust to strong occlusions with a pose accuracy below 10mm up to 40% occlusion. Although the surgeon HMD provided one of the most beneficial perspectives on un-occluded frames, in our experiments the small FOV of the HL 2 PV camera resulted in frequent and heavy truncation of the instruments, which significantly decreased the average pose accuracy. In contrast, the perspectives of both static cameras opposite of the surgeon are consistently among the most favorable for the pose estimation task.

Using multiple views for pose estimation resulted in a 10-

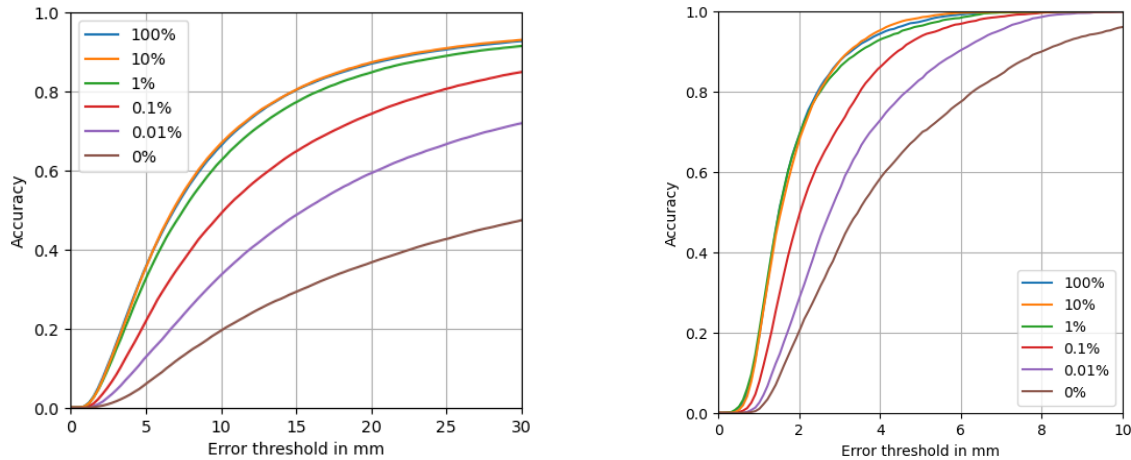


Fig. 13: Influence of the amount of real training data, evaluated for SurfEmb (left) and EpiSurfEmb with five static cameras (right) on the wet lab dataset. All models were trained with a fraction of the real training set and the complete synthetic training set. We observe no significant performance drop with as little as 1% of the real training samples. The curves for 100% and 10% are almost identical.

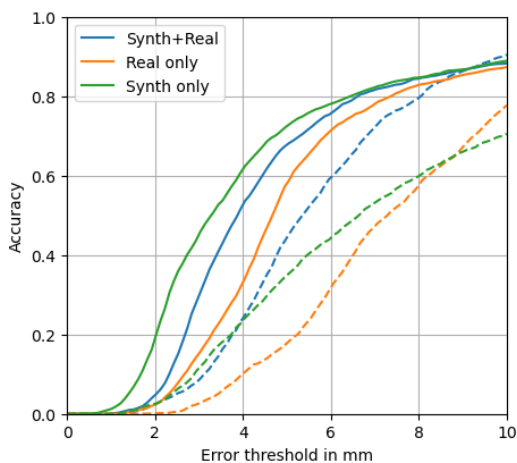


Fig. 14: ADD accuracy-threshold curves of EpiSurfEmb with five views on the OR-X test set. The results on the bright subset are indicated with solid lines; results on the dark subset are shown as dashed lines.

fold improvement in position accuracy compared to the single-view baselines, which is in line with the findings by Haugaard and Iversen (2023). The results on the wet lab dataset show that position and orientation errors as low as 1.01 mm and 0.89° can be achieved when the test-time camera configuration is known and the model is refined on in-domain data. The camera configuration consisting of the two cameras opposite of the surgeon consistently outperformed all other configurations of two cameras and achieved a similar pose accuracy as the best overall configuration with five cameras. These findings highlight that highly accurate and marker-less pose estimation is already within reach with two well-placed cameras.

However, our wet lab dataset was recorded in a controlled environment that is arguably less cluttered than a real operation room. The benefits of using configurations comprising more than two cameras are expected to be more noticeable in cluttered environments, where cameras are frequently occluded. As such, our results should be interpreted with an understanding that they indicate the minimum number of unoccluded views

necessary to achieve a certain pose accuracy, rather than an absolute quantification of the number of cameras. Similarly, wide-FOV HMDs will be able to show their advantages in more cluttered environments where static cameras are more prone to occlusions (Saito *et al.*, 2021).

The evaluations on the OR-X test set highlight that synthetic data with controllable and diverse image distributions are important to train robust models that can generalize to different camera setups, i.e. when the test-time conditions are unknown. In our experiments, complementing our synthetic data set with only 12 k real samples was sufficient to reach a similar performance as training with 100× more real samples. However, the worse pose accuracy on the OR-X test set indicates that in-domain data is still necessary to satisfy the high clinical requirements. Improvements in the generation of synthetic images could further reduce these requirements. For example, rendering synthetic images based on a known test-time camera configuration for model refinement may result in more accurate pose estimates than sampling from a uniform pose distribution.

Compared to the results on the surgical wet lab dataset, the evaluations on the OR-X test set show an expected decrease in pose accuracy, which can be partially attributed to the larger scale of the ceiling-mounted camera setup. This performance decrease can be avoided by using cameras with a higher optical zoom. Although this is not possible with Azure Kinect cameras, we retained them in our experiments to assess the potential of using depth information. Higher optical zooms for RGB cameras are widely available and could increase the pixel density in the surgeon’s working volume.

4.1. Dataset

Beyond instrument pose estimation, the rich annotations and modalities provided with our dataset can be utilized for several related tasks such as hand or joint hand-object pose estimation and tracking (Hein *et al.*, 2021; Wang *et al.*, 2023), reconstruction (Leng *et al.*, 2023), or novel view synthesis (Mildenhall *et al.*, 2021; Truong *et al.*, 2023). In the clinical context, our dataset can serve as the basis for surgical behavioral and in-

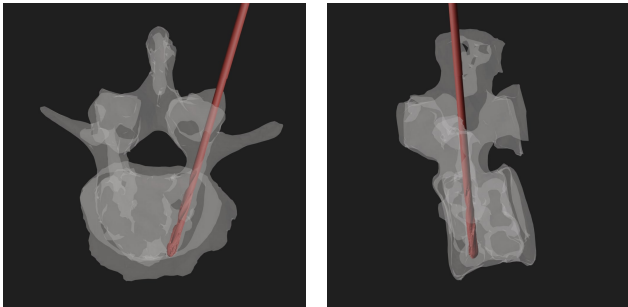


Fig. 15: Superior and lateral view of an exemplary drill trajectory inside the L4 vertebra.

teraction models based on the provided instrument-, hand- and anatomy poses and eye gaze information displayed in Figures 2 and 15. Moreover, the instrument and anatomy information can be used to render digitally reconstructed radiographs of realistic instrument trajectories, enabling the training of pose estimation and phase detection models in the x-ray domain (Kügler *et al.*, 2020; Killeen *et al.*, 2023).

4.2. Limitations

Our work has several limitations. First, the use of a single clinical-grade marker-based tracking system for ground truth data capture prevents a comprehensive comparison of the robustness of marker-based and marker-less methods, as no secondary source of ground truth poses is available when tracking is lost. We found that a significant fraction of frames had to be discarded due to line-of-sight issues. While we cannot evaluate the performance of our system on these frames due to the lack of ground truth annotations, the pose estimates of the marker-less baselines have a great visual overlap, as shown in Figure 16. We decided against additional tracking systems despite the increased effective working volume and reduced occlusion issues, to limit interferences between the tracking system and depth sensors in the IR spectrum. Still, multiple tracking systems could be deployed in combination with stereo RGB cameras or sensors that utilize different wavelengths, potentially coupled with matching IR filters.

Second, the hemispherical fiducials can introduce a triangulation error during the regression of the detected blob centers due to the asymmetric shape of their projections. We observed that the screwdriver’s pose annotations are less accurate than the drill’s pose annotations due to the more challenging placement and detection of the marker array. Thus, the worse accuracy of the screwdriver’s pose estimates might be partially caused by a less accurate ground truth. The accuracy of the ground truth could be improved using larger spherical or disk-shaped fiducials. However, large visible markers increase the risk of models overfitting to the marker. Alternatively, a robot-based capture setup could alleviate the need for markers.

Third, our dataset does not capture instrument articulations but assumes full rigidity, since marker-based tracking of all articulations is complex and impractical. As a result, the ground truth 2D-3D correspondences extracted on the affected regions can be incorrect and may prevent models from fully utilizing

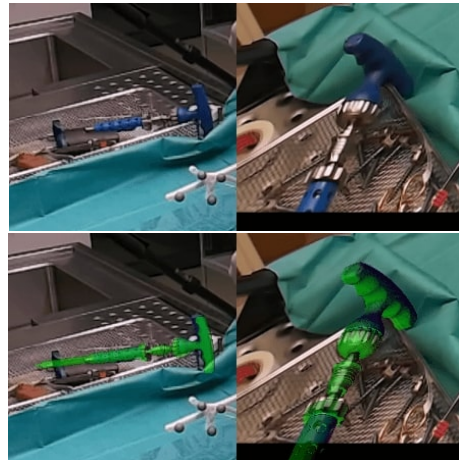


Fig. 16: In the shown frames the marker-based tracking failed because the instrument is located outside the working volume, while the proposed marker-less multi-camera system remains functional. The top row shows the two input RGB patches while the bottom row highlights the estimated pose. The image patches were manually cropped for these frames, as no ground truth annotations are available. The large visual overlap indicates that the pose estimate is accurate even with only two views.

the local shape and texture information. In contrast to marker-based approaches, learning-based models can be extended to explicitly model articulations in the future.

Last, occlusion patterns in ex-vivo surgeries are less complex compared to corresponding in-vivo surgeries, due to the limited staff and instruments present. An analysis of real surgeries and different interventions is necessary to verify our findings on realistic occlusion patterns.

4.3. Conclusion

Our study showcased how a dedicated computer vision setup for surgery can enhance current capabilities in surgical navigation and instrument tracking. The comprehensive and systematic evaluation will bring us one step closer to transferring such systems into everyday clinical practice.

A main finding concerning accuracy is that marker-less and millimeter-accurate pose estimation is attainable with as little as two cameras, demonstrating that marker-less tracking is becoming a feasible alternative to existing marker-based systems. Furthermore, we show that if the test-time camera configuration is known, refinement on real in-domain data can further reduce pose errors to 1.01 mm and 0.89° under optimal conditions. In addition, our results show that synthetic data is important to obtain more robust models, which is particularly relevant in a largely dynamic and varying environment such as surgery.

Nevertheless, there are still surgical applications with accuracy requirements in the sub-millimeter range (Rampersaud *et al.*, 2001). Further research is needed to improve the pose estimation accuracy and robustness, especially for minimal camera setups and mobile cameras. Potential improvements include the explicit modeling of articulations, the temporal integration of 2D-3D correspondences, and a pose uncertainty estimation. Moreover, capturing the characteristics of a known test-time environment to generate similar synthetic data could further reduce the need for a time-consuming collection of annotated in-

domain data. Last, determining the occlusion patterns during real surgeries is highly relevant to finding optimal camera configurations that satisfy the clinical requirements for accuracy and robustness, while maximizing space efficiency.

We envision our setup as a prototype for robust markerless optical 6DoF tracking systems in the future trajectory of surgery, and that our dataset accelerates further research in this direction.

Declaration of competing interest

The authors declare the following financial interests/personal relationships which may be considered as potential competing interests: Mazda Farshad reports a relationship with Incomed AG and X23D AG that includes: board membership and equity or stocks. Philipp Frnstahl reports a relationship with X23D AG that includes: board membership and equity or stocks.

Data availability

The dataset will be made available on our project page <https://jonashein.github.io/mvpsp/>.

CRedit authorship contribution statement

Jonas Hein: Conceptualization, Methodology, Software, Validation, Formal analysis, Investigation, Data Curation, Writing - Original Draft, Visualization. **Nicola Cavalcanti:** Investigation. **Daniel Suter:** Investigation. **Lukas Zingg:** Investigation. **Fabio Carrillo:** Writing - Review & Editing. **Lilian Calvet:** Writing - Review & Editing. **Mazda Farshad:** Resources. **Nassir Navab:** Supervision. **Marc Pollefeys:** Resources, Supervision, Funding acquisition. **Philipp Frnstahl:** Resources, Writing - Review & Editing, Supervision, Project administration, Funding acquisition.

Acknowledgements

This work has been supported by OR-X - a Swiss national research infrastructure for translational surgery and associated funding by the University Hospital Balgrist, as well as by the InnoSuisse PROFICIENCY grant. The study was conducted according to the guidelines of the Declaration of Helsinki, and approved by the local ethical committee (KEK Zurich BASEC No. 2017-00874 and 2021-01196). We like to thank Haugaard and Iversen (2023) for providing a reference implementation, as well as Olivia Bossert and Frdric Giraud for their support during the data capture.

References

- Allan, M., Chang, P.L., Ourselin, S., Hawkes, D.J., Sridhar, A., Kelly, J., Stoyanov, D., 2015. Image based surgical instrument pose estimation with multi-class labelling and optical flow, in: Medical Image Computing and Computer-Assisted Intervention-MICCAI 2015: 18th International Conference, Munich, Germany, October 5-9, 2015, Proceedings, Part I 18, Springer. pp. 331-338.
- Allan, M., Kondo, S., Bodenstedt, S., Leger, S., Kadkhodamohammadi, R., Luengo, I., Fuentes, F., Flouty, E., Mohammed, A., Pedersen, M., et al., 2020. 2018 robotic scene segmentation challenge. arXiv preprint arXiv:2001.11190.
- Barath, D., Matas, J., 2019. Progressive-x: Efficient, anytime, multi-model fitting algorithm, in: Proceedings of the IEEE/CVF international conference on computer vision, pp. 3780-3788.
- Bouget, D., Allan, M., Stoyanov, D., Jannin, P., 2017. Vision-based and markerless surgical tool detection and tracking: a review of the literature. Medical image analysis 35, 633-654.
- Chiu, Z.Y., Liao, A.Z., Richter, F., Johnson, B., Yip, M.C., 2022. Markerless suture needle 6d pose tracking with robust uncertainty estimation for autonomous minimally invasive robotic surgery, in: 2022 IEEE/RSJ International Conference on Intelligent Robots and Systems (IROS), IEEE. pp. 5286-5292.
- Chum, O., Matas, J., Kittler, J., 2003. Locally optimized ransac, in: Joint Pattern Recognition Symposium, Springer. pp. 236-243.
- Denninger, M., Winkelbauer, D., Sundermeyer, M., Boerdijk, W., Knauer, M., Strobl, K.H., Humt, M., Triebel, R., 2023. Blenderproc2: A procedural pipeline for photorealistic rendering. Journal of Open Source Software 8, 4901. URL: <https://doi.org/10.21105/joss.04901>.
- Doughty, M., Ghugre, N.R., 2022. Hmd-egopose: Head-mounted display-based egocentric marker-less tool and hand pose estimation for augmented surgical guidance. International Journal of Computer Assisted Radiology and Surgery 17, 2253-2262.
- Fang, Y., Liao, B., Wang, X., Fang, J., Qi, J., Wu, R., Niu, J., Liu, W., 2021. You only look at one sequence: Rethinking transformer in vision through object detection. Advances in Neural Information Processing Systems 34, 26183-26197.
- Farshad, M., Frnstahl, P., Spirig, J.M., 2021. First in man in-situ augmented reality pedicle screw navigation. North American Spine Society Journal (NASSJ) 6, 100065.
- Feuner, H., Park, A., 2017. Surgery 4.0: the natural culmination of the industrial revolution? Innovative Surgical Sciences 2, 105-108.
- Garrow, C.R., Kowalewski, K.F., Li, L., Wagner, M., Schmidt, M.W., Engelhardt, S., Hashimoto, D.A., Kenngott, H.G., Bodenstedt, S., Speidel, S., et al., 2021. Machine learning for surgical phase recognition: a systematic review. Annals of surgery 273, 684-693.
- Girardi, F., Cammisa, F., Sandhu, H., 1999. The placement of lumbar pedicle screws using computerised stereotactic guidance. The Journal of Bone & Joint Surgery British Volume 81, 825-829.
- Haidegger, T., Speidel, S., Stoyanov, D., Satava, R.M., 2022. Robot-assisted minimally invasive surgery—surgical robotics in the data age. Proceedings of the IEEE 110, 835-846.
- Hrtl, R., Lam, K.S., Wang, J., Korge, A., Kandziora, F., Audig, L., 2013. Worldwide survey on the use of navigation in spine surgery. World neurosurgery 79, 162-172.
- Hasan, M.K., Calvet, L., Rabbani, N., Bartoli, A., 2021. Detection, segmentation, and 3d pose estimation of surgical tools using convolutional neural networks and algebraic geometry. Medical Image Analysis 70, 101994.
- Haugaard, R.L., Buch, A.G., 2022. Surfemb: Dense and continuous correspondence distributions for object pose estimation with learnt surface embeddings, in: Proceedings of the IEEE/CVF Conference on Computer Vision and Pattern Recognition, pp. 6749-6758.
- Haugaard, R.L., Hagelskjr, F., Iversen, T.M., 2023. Spyropose: Se (3) pyramids for object pose distribution estimation, in: Proceedings of the IEEE/CVF International Conference on Computer Vision, pp. 2082-2091.
- Haugaard, R.L., Iversen, T.M., 2023. Multi-view object pose estimation from correspondence distributions and epipolar geometry, in: 2023 IEEE International Conference on Robotics and Automation (ICRA), IEEE. pp. 1786-1792.
- Hein, J., Seibold, M., Bogo, F., Farshad, M., Pollefeys, M., Frnstahl, P., Navab, N., 2021. Towards markerless surgical tool and hand pose estimation. International journal of computer assisted radiology and surgery 16, 799-808.
- Hinterstoisser, S., Lepetit, V., Ilic, S., Holzer, S., Bradski, G., Konolige, K., Navab, N., 2012. Model based training, detection and pose estimation of texture-less 3d objects in heavily cluttered scenes, in: Asian conference on computer vision, Springer. pp. 548-562.
- Hodan, T., Michel, F., Brachmann, E., Kehl, W., GlentBuch, A., Kraft, D., Drost, B., Vidal, J., Ihrke, S., Zabulis, X., et al., 2018. Bop: Benchmark for 6d object pose estimation, in: Proceedings of the European conference on computer vision (ECCV), pp. 19-34.

- Hu, Y., Speierer, S., Jakob, W., Fua, P., Salzmann, M., 2021. Wide-depth-range 6d object pose estimation in space, in: Proceedings of the IEEE/CVF Conference on Computer Vision and Pattern Recognition, pp. 15870–15879.
- Joskowicz, L., Hazan, E.J., 2016. Computer aided orthopaedic surgery: incremental shift or paradigm change? *Medical image analysis* 33, 84–90.
- Killeen, B.D., Zhang, H., Mangulabnan, J., Armand, M., Taylor, R.H., Osgood, G., Unberath, M., 2023. Pelphix: Surgical phase recognition from x-ray images in percutaneous pelvic fixation, in: International Conference on Medical Image Computing and Computer-Assisted Intervention, Springer. pp. 133–143.
- Kügler, D., Sehring, J., Stefanov, A., Stenin, I., Kristin, J., Klenzner, T., Schipper, J., Mukhopadhyay, A., 2020. I3posnet: instrument pose estimation from x-ray in temporal bone surgery. *International journal of computer assisted radiology and surgery* 15, 1137–1145.
- Labbé, Y., Carpentier, J., Aubry, M., Sivic, J., 2020. Cosypose: Consistent multi-view multi-object 6d pose estimation, in: European Conference on Computer Vision, Springer. pp. 574–591.
- Lam, K., Chen, J., Wang, Z., Iqbal, F.M., Darzi, A., Lo, B., Purkayastha, S., Kinross, J.M., 2022. Machine learning for technical skill assessment in surgery: a systematic review. *NPJ digital medicine* 5, 1–16.
- Lee, S.C., Fuerst, B., Taten, K., Johnson, A., Fotouhi, J., Osgood, G., Tombari, F., Navab, N., 2017. Multi-modal imaging, model-based tracking, and mixed reality visualisation for orthopaedic surgery. *Healthcare technology letters* 4, 168–173.
- Leng, Z., Wu, S.C., Saleh, M., Montanaro, A., Yu, H., Wang, Y., Navab, N., Liang, X., Tombari, F., 2023. Dynamic hyperbolic attention network for fine hand-object reconstruction, in: Proceedings of the IEEE/CVF International Conference on Computer Vision, pp. 14894–14904.
- Liebmann, F., von Atzigen, M., Stütz, D., Wolf, J., Zingg, L., Suter, D., Cavalcanti, N.A., Leoty, L., Esfandiari, H., Snedeker, J.G., et al., 2023. Automatic registration with continuous pose updates for marker-less surgical navigation in spine surgery. *Medical Image Analysis* , 103027.
- Liebmann, F., Stütz, D., Suter, D., Jecklin, S., Snedeker, J.G., Farshad, M., Fürnstahl, P., Esfandiari, H., 2021. Spinedepth: A multi-modal data collection approach for automatic labelling and intraoperative spinal shape reconstruction based on rgb-d data. *Journal of Imaging* 7, 164.
- Liu, Y., Wen, Y., Peng, S., Lin, C., Long, X., Komura, T., Wang, W., 2022. Gen6d: Generalizable model-free 6-dof object pose estimation from rgb images, in: European Conference on Computer Vision, Springer. pp. 298–315.
- Luther, N., Iorgulescu, J.B., Geannette, C., Gebhard, H., Saleh, T., Tsiouris, A.J., Härtl, R., 2015. Comparison of navigated versus non-navigated pedicle screw placement in 260 patients and 1434 screws. *Journal of Spinal Disorders and Techniques* 28, E298–E303.
- Maier-Hein, L., Eisenmann, M., Sarikaya, D., März, K., Collins, T., Malpani, A., Fallert, J., Feussner, H., Giannarou, S., Mascagni, P., et al., 2022. Surgical data science—from concepts toward clinical translation. *Medical image analysis* 76, 102306.
- Mascagni, P., Alapatt, D., Sestini, L., Altieri, M.S., Madani, A., Watanabe, Y., Alseidi, A., Redan, J.A., Alfieri, S., Costamagna, G., et al., 2022. Computer vision in surgery: from potential to clinical value. *npj Digital Medicine* 5, 163.
- Mildenhall, B., Srinivasan, P.P., Tancik, M., Barron, J.T., Ramamoorthi, R., Ng, R., 2021. Nerf: Representing scenes as neural radiance fields for view synthesis. *Communications of the ACM* 65, 99–106.
- Movshovitz-Attias, Y., Kanade, T., Sheikh, Y., 2016. How useful is photo-realistic rendering for visual learning?, in: Computer Vision—ECCV 2016 Workshops: Amsterdam, The Netherlands, October 8–10 and 15–16, 2016, Proceedings, Part III 14, Springer. pp. 202–217.
- Özsoy, E., Czempiel, T., Örnek, E.P., Eck, U., Tombari, F., Navab, N., 2023. Holistic or domain modeling: a semantic scene graph approach. *International Journal of Computer Assisted Radiology and Surgery* , 1–9.
- Özsoy, E., Örnek, E.P., Eck, U., Czempiel, T., Tombari, F., Navab, N., 2022. 4d-or: Semantic scene graphs for or domain modeling, in: Medical Image Computing and Computer Assisted Intervention—MICCAI 2022: 25th International Conference, Singapore, September 18–22, 2022, Proceedings, Part VII, Springer. pp. 475–485.
- Perdomo-Pantoja, A., Ishida, W., Zygorakis, C., Holmes, C., Iyer, R.R., Cottrill, E., Theodore, N., Witham, T.F., Sheng-fu, L.L., 2019. Accuracy of current techniques for placement of pedicle screws in the spine: a comprehensive systematic review and meta-analysis of 51,161 screws. *World neurosurgery* 126, 664–678.
- Qiu, L., Li, C., Ren, H., 2019. Real-time surgical instrument tracking in robot-assisted surgery using multi-domain convolutional neural network. *Healthcare technology letters* 6, 159–164.
- Rampersaud, Y.R., Simon, D.A., Foley, K.T., 2001. Accuracy requirements for image-guided spinal pedicle screw placement. *Spine* 26, 352–359.
- Redmon, J., Farhadi, A., 2018. Yolov3: An incremental improvement. *arXiv preprint arXiv:1804.02767* .
- Saito, Y., Hachiuma, R., Saito, H., Kajita, H., Takatsume, Y., Hayashida, T., 2021. Camera selection for occlusion-less surgery recording via training with an egocentric camera. *IEEE Access* 9, 138307–138322.
- Sarikaya, D., Corso, J.J., Guru, K.A., 2017. Detection and localization of robotic tools in robot-assisted surgery videos using deep neural networks for region proposal and detection. *IEEE transactions on medical imaging* 36, 1542–1549.
- Shugurov, I., Zakharov, S., Ilic, S., 2021. Dpodv2: Dense correspondence-based 6 dof pose estimation. *IEEE transactions on pattern analysis and machine intelligence* 44, 7417–7435.
- Smith, L.N., 2018. A disciplined approach to neural network hyper-parameters: Part 1—learning rate, batch size, momentum, and weight decay. *arXiv preprint arXiv:1803.09820* .
- Speidel, S., Maier-Hein, L., Stoyanov, D., Bodenstedt, S., Reinke, A., Bano, S., Jenke, A., Wagner, M., Daum, M., Tabibian, A., Das, A., Zhang, Y., Vasconcelos, F., Psychogyios, D., Khan, D.Z., Marcus, H.J., Zia, A., Liu, X., Bhattacharyya, K., Wang, Z., Berniker, M., Perreault, C., Jarc, A., Malpani, A., Glock, K., Xu, H., Xu, C., Huang, B., Giannarou, S., 2023. Endoscopic Vision Challenge 2023. URL: <https://doi.org/10.5281/zenodo.8315050>, doi:10.5281/zenodo.8315050.
- Su, Y., Saleh, M., Fetzer, T., Rambach, J., Navab, N., Busam, B., Stricker, D., Tombari, F., 2022. Zebrapose: Coarse to fine surface encoding for 6dof object pose estimation, in: Proceedings of the IEEE/CVF Conference on Computer Vision and Pattern Recognition, pp. 6738–6748.
- Tommasi, T., Patricia, N., Caputo, B., Tuytelaars, T., 2017. A deeper look at dataset bias. *Domain adaptation in computer vision applications* , 37–55.
- Torralba, A., Efros, A.A., 2011. Unbiased look at dataset bias, in: CVPR 2011, IEEE. pp. 1521–1528.
- Truong, P., Rakotosaona, M.J., Manhardt, F., Tombari, F., 2023. Sparf: Neural radiance fields from sparse and noisy poses, in: Proceedings of the IEEE/CVF Conference on Computer Vision and Pattern Recognition, pp. 4190–4200.
- Virk, S., Qureshi, S., 2019. Navigation in minimally invasive spine surgery. *Journal of Spine Surgery* 5, S25.
- Wang, C., Xu, D., Zhu, Y., Martín-Martín, R., Lu, C., Fei-Fei, L., Savarese, S., 2019. Densefusion: 6d object pose estimation by iterative dense fusion, in: Proceedings of the IEEE/CVF conference on computer vision and pattern recognition, pp. 3343–3352.
- Wang, G., Manhardt, F., Tombari, F., Ji, X., 2021. GDR-Net: Geometry-guided direct regression network for monocular 6d object pose estimation, in: IEEE/CVF Conference on Computer Vision and Pattern Recognition (CVPR), pp. 16611–16621.
- Wang, R., Ktistakis, S., Zhang, S., Meboldt, M., Lohmeyer, Q., 2023. Povsurgery: A dataset for egocentric hand and tool pose estimation during surgical activities, in: International Conference on Medical Image Computing and Computer-Assisted Intervention, pp. 440–450.
- Xiang, Y., Schmidt, T., Narayanan, V., Fox, D., 2018. Posecnn: A convolutional neural network for 6d object pose estimation in cluttered scenes.
- Zhang, Z., 2000. A flexible new technique for camera calibration. *IEEE Transactions on pattern analysis and machine intelligence* 22, 1330–1334.
- Zhao, Z., Chen, Z., Voros, S., Cheng, X., 2019. Real-time tracking of surgical instruments based on spatio-temporal context and deep learning. *Computer Assisted Surgery* 24, 20–29.

Appendix

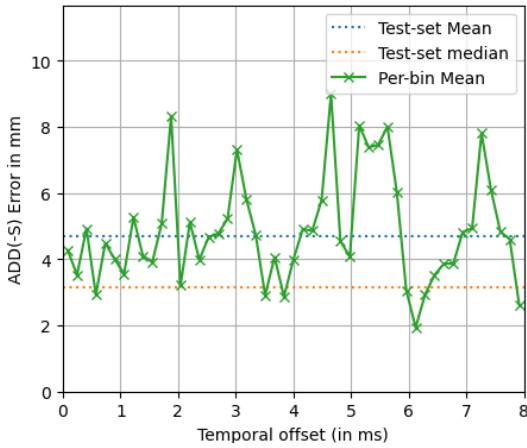


Fig. A.1: The influence of the temporal offset on the ADD(-S) error is negligible. We average the ADD(-S) error within 50 bins of equal width. Temporal offsets below 50 μ s are not included.



Fig. A.2: Exemplary frame of SurfEmb’s depth refinement step largely sampling from occluded pixels, in this case on the surgeon’s hand. The left image shows the input RGB patch with the selected pixels highlighted. The right image shows the predicted query image, where brighter colors indicate a larger norm. The red dot indicates the ray along which the pose is refined.

HMD Temporal Synchronization. To exclude any synchronization issues as the reason for the lower pose estimation accuracy of the HMDs, we compared the ADD(-S) errors of EpiSurfEmb on all 2-view camera configurations to the corresponding temporal offset between the exposure windows of the two input RGB images. As displayed in Figure A.1, we did not find any significant correlation between the two variables.

SurfEmb Depth Refinement. SurfEmb’s depth refinement step does not consistently improve the pose accuracy on our dataset. We found that this refinement can often improve the pose accuracy significantly, but it lacks robustness to partial occlusions. The method assumes that pixels with a high query norm (i.e. $> 80\%$ of the maximum query norm in the image) are not occluded, as the model is most certain about them. This assumption often does not hold, leading to the majority of pixels being sampled from the surgeon’s hand. In addition, the selected pixels are often focused around a single point, instead of being



Fig. A.3: The sampled pixels for the depth refinement can be placed suboptimally. The left image shows an exemplary RGB patch, where the selected pixels for the depth refinement are focused around a thin and metallic part of the screwdriver. The right image shows the captured depth image, which does not fully capture the instrument’s shape. Note that the center of the instrument appears thinner than it is, while some pixels erroneously contain the depth of the background.

distributed on the instrument surface. As a result, the method is less robust to partial occlusions. A representative example is shown in Figure A.2.

In some cases, the depth sensor fails to perceive thin or metallic surfaces and erroneously measures the depth of the background. An exemplary frame is shown in Figure A.3. Moreover, we observe that the depth measurements can be inaccurate depending on the normal of the reflecting surface and lighting conditions.

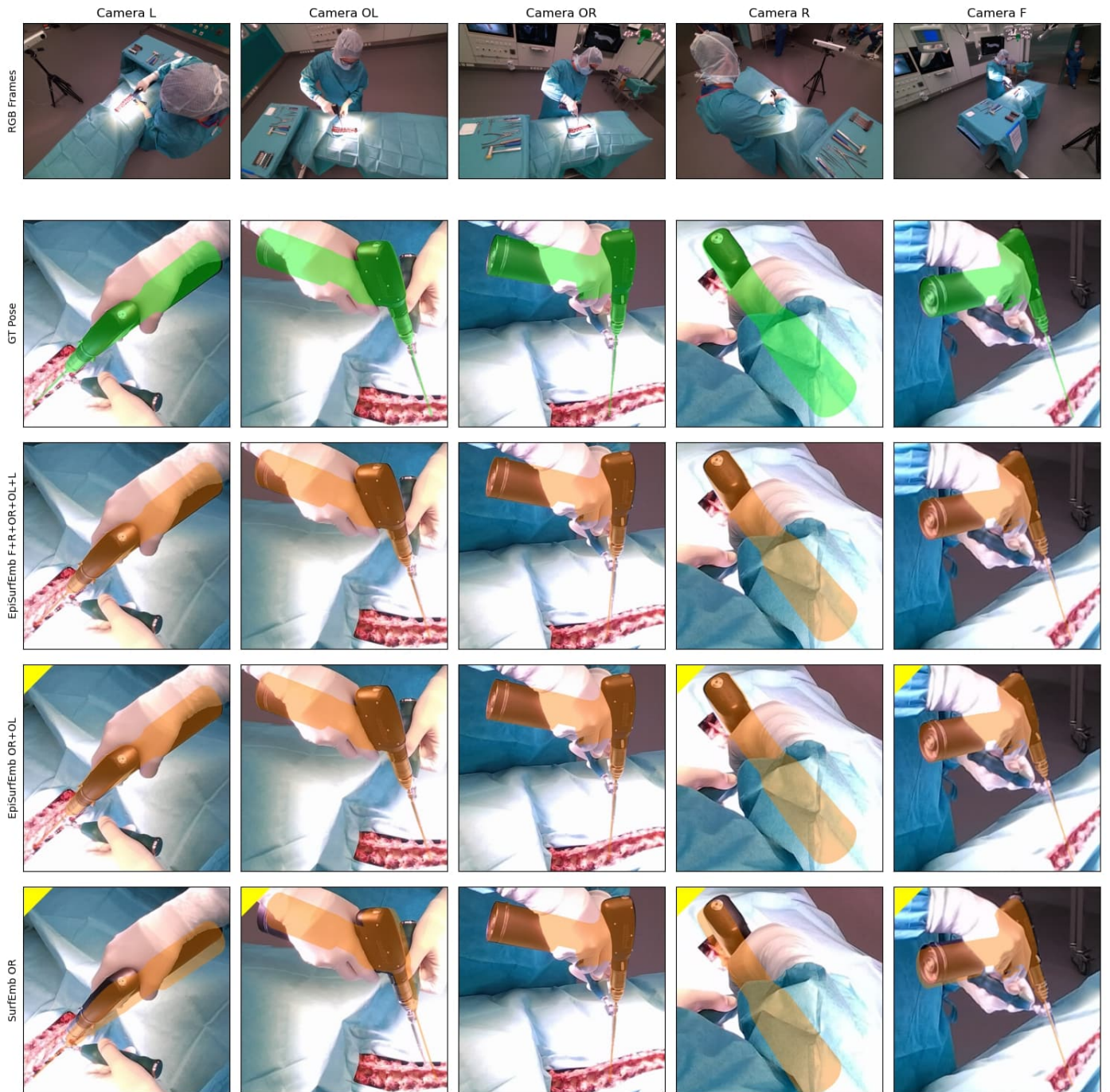


Fig. A.4: Qualitative Comparison of the best single-view, two-view, and five-view baselines on the OR-X bright subset. We superimpose the ground truth pose in green in the second row and pose estimates in orange in the following rows. Yellow triangles in the top-left image corners indicate that the frame was not part of the input to the pose estimation method. Note that the single-view pose estimate has a great visual overlap on the input image, but a significant error when viewed from other perspectives due to the depth ambiguity.



Fig. A.5: Qualitative Comparison of the best single-view, two-view, and five-view baselines on the OR-X dark subset. We superimpose the ground truth pose in green in the second row and pose estimates in orange in the following rows. Yellow triangles in the top-left image corners indicate that the frame was not part of the input to the pose estimation method. Note that the single-view pose estimate has a great visual overlap on the input image, but a significant error when viewed from other perspectives due to the depth ambiguity.

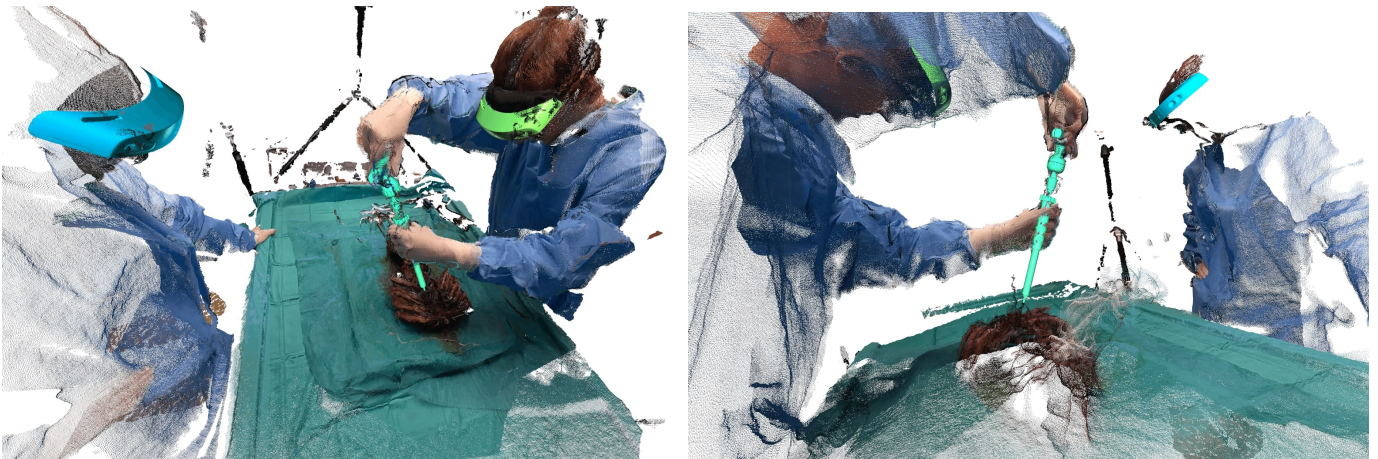


Fig. A.6: Visualization of the colored point clouds from all cameras in the wet lab dataset. We overlay and highlight the 3D models of both tracked HMDs and the instrument.